Estimation of Atlantic Tropical Cyclone Rainfall Frequency in the United States

MONIKA FELDMANN

Massachusetts Institute of Technology, Cambridge, Massachusetts, and Eidgenössiche Technische Hochschule Zürich, Zurich, and Ecole Polytechnique Fédérale de Lausanne, Lausanne, Switzerland

KERRY EMANUEL

Massachusetts Institute of Technology, Cambridge, Massachusetts

LAIYIN ZHU

Western Michigan University, Kalamazoo, Michigan

ULRIKE LOHMANN

Eidgenössiche Technische Hochschule Zürich, Zurich, Switzerland

(Manuscript received 23 January 2019, in final form 14 May 2019)

ABSTRACT

Tropical cyclones pose a significant flood risk to vast land regions in their path because of extreme precipitation. Thus it is imperative to quantitatively assess this risk. This study compares exceedance frequencies of tropical cyclone precipitation derived from two independent observational datasets with those estimated using a tropical cyclone rainfall algorithm applied to large sets of synthetic tropical cyclones. The modeled rainfall compares reasonably well to observed rainfall across much of the southern United States but does less well in the mid-Atlantic states. Possible causes of this disparity are discussed.

1. Introduction

Tropical cyclones (TCs) contribute approximately 3% to precipitation in low and midlatitudes. For coastal areas prone to TCs, this fraction increases to 15%–45% of all precipitation (Jiang and Zipser 2010). Moreover, TCs inflict large financial losses, which have been increasing and are likely to continue doing so (Peduzzi et al. 2012). The increase is linked to economic development in coastal areas, rather than climatological factors, as the nominalized damage of TCs remains without trend (Weinkle et al. 2018). Precipitation and the resulting freshwater flooding are also one of the leading causes of fatalities in TCs; indeed, 27% have been attributed to freshwater flooding, whereas wind, including tornadoes in TCs, was responsible for only 11% of fatalities (Rappaport 2014).

Precipitation forms in different regions of a TC. The highest rain rates are found in the eyewall, where the strongest convection takes place. Outside the eyewall, precipitation is concentrated into spiral rainbands that wind outward from the center of the TC. No precipitation forms in the mostly clear eye, as it is a region of subsidence (Houze 2014). The heavy precipitation of TCs is mainly caused by strong updrafts that advect moisture upward from the boundary layer.

The intensity of precipitation throughout the storm is linked to the intensity of the secondary circulation, which is proportional to the intensity of the TC and its rate of intensification, as the increasing diabatic heating drives the secondary circulation and thus the updrafts (Yu et al. 2017). However, at a fixed point under the

Denotes content that is immediately available upon publication as open access.

Supplemental information related to this paper is available at the Journals Online website: https://doi.org/10.1175/JAMC-D-19-0011.s1.

Corresponding author: Monika Feldmann, monika.feldmann@alumni.ethz.ch

DOI: 10.1175/JAMC-D-19-0011.1

influence of a TC, the storm total precipitation is as much a function of the duration of the storm as of its intensity. The larger a TC and the slower its translational speed are, the larger is the storm total precipitation (Matyas 2010).

A recent case was Hurricane Harvey, which made landfall in August 2017 in Texas. Its extreme precipitation of more than 1000 mm (Blake and Zelinsky 2018) made Harvey the wettest TC on record in the United States (Roth 2018), largely because it stalled over the Texas' coastal region for 4 days. Its combined wind, rain, and storm surge led to direct economic damage currently estimated at up to U.S. $95 billion (Munich Re 2018).

A more recent example is Hurricane Florence, which made landfall in North Carolina in September 2018. With precipitation peaks of more than 700 mm, it broke the records of storm total precipitation of a single storm in the Carolinas (National Weather Service 2018). The previously wet summer exacerbated the flood risk, as the soil was already close to saturation. The resulting widespread flooding caused U.S. $14 billion in damage (Faust and Bove 2018).

Risser and Wehner (2017) and van Oldenborgh et al. (2017) recently analyzed extreme precipitation, including TCs, in the Gulf of Mexico region. They estimated the change in return periods of extreme precipitation events over the last century using rain gauge, radar, and model data. While their analyses included approximately 30% extreme precipitation events that are not associated with TCs, they both show a clear upward trend in the frequency of extreme precipitation. They ascribed this trend mainly to anthropogenic climate change. This is well in line with Emanuel (2017), who estimated the trend in model-simulated return periods of extreme precipitation events associated with TCs near Houston using the modeling approach we apply here. In this approach, a tropical cyclone rainfall algorithm (hereinafter TCR) is applied to tropical cyclone model output to estimate the distribution and magnitude of TC rainfall.

The results of applying this modeling approach to synthetic TC tracks were compared with 60 yr of rain gauge data along the coast of Texas by Zhu and Quiring (2013). Lu et al. (2018) applied the TCR to WRF Model output and compared the resulting rainfall with the precipitation produced directly by the WRF Model. In both cases, the TCR performed very well. Here we use observational records from ~25 yr of radar and ~95 yr of rain gauge data to evaluate a revised TC precipitation algorithm applied to large sets of synthetic TC tracks affecting the United States. By extending the study of Zhu and Quiring (2013), we aim both to improve the rainfall algorithm and to provide a thorough analysis of the TCR performance along the entire U.S. Atlantic coastline.

2. Data

We develop TC precipitation climatologies using both rain gauge and radar data. Several data sources were used to accomplish this: radar data from the NEXRAD radar network (NCEI 2018a), rain gauge data from an existing TC-precipitation dataset (Zhu and Quiring 2017, 2013) and historical TC data from IBTrACS (Knapp et al. 2010) and Colorado State University (Demuth et al. 2006). We then compare these climatologies with those derived from the application of a revised TCR algorithm to large sets of synthetic TC tracks.

a. Historical TC (best track) data

We obtain North Atlantic historical TC data from IBTrACS, a global compilation of TC records (Knapp et al. 2010). It provides TC positions, wind speed, sea level pressure and, since 2001, TC size metrics, with 3-hourly resolution. The extended best-track archive from Colorado State University (Demuth et al. 2006) additionally contains TC size data from 1988 to 2016 (as of May 2018) in a 6-hourly resolution. The IBTrACS record and the extended best-track archive are merged to create a new TC track record beginning in the early twentieth century, including TC size metrics since 1988. As discussed in section 3a, the radius of outermost closed isobar (ROCI) is used to determine the TC size. Where the ROCI was not available, the median of all available ROCI (~334 km) is assumed.

b. NEXRAD radar data

The U.S. radar network covers vast parts of the continental United States with 159 S-band Doppler radars, providing a comprehensive resource for precipitation data (NCEI 2018b). The observational time series for storms extends back to 1992 (NCEI 2018b) and provide data at a spatial resolution of initially $1° \times 2$ km on a polar grid, where the radial resolution improved over time (Smith et al. 1996; NCEI 2018b). When transforming the data to a coordinate grid, a uniform resolution of $0.1° \times 0.1°$ was chosen. In this step the data are resampled using a nearest-neighbor technique (NCEI 2019).

The NEXRAD stage III radar data are processed with a precipitation processing system (Office of the Federal Coordinator for Meteorological Services and Supporting Research 2017) that produces precipitation products from the measured reflectivity values while applying quality adjustments such as accounting for ground clutter and beam attenuation. For this analysis,

the running hourly precipitation accumulations at 37 selected stations were used. The data are archived with varying temporal resolutions of 4–60 min, depending on the weather situation (Smith et al. 1996). When interpolated, the data provide time-evolving accumulated precipitation over the observed area. Since this is a running total, the overlap of data also reduces issues stemming from missing single measurements.

The main advantage of radar measurements is their high resolution in space and time. As TC precipitation is highly variable in space and time, high resolution is needed for obtaining accurate estimates of precipitation.

Radar measurements themselves contain uncertainties. Because of the curvature of Earth and the elevation of the beam, measurements farther away from the radar are taken at a higher altitude. Inferring precipitation at the ground from measurements at altitude introduces errors, which are magnified when the radar beam extends into the melting layer, which requires a different precipitation–reflectivity relationship (Wilson and Brandes 1979). Attenuation of radar radiation in heavy precipitation is also problematic (Curry 2012). Owing to the expansion of the radar beam, the spatial resolution of the measurements decreases with increasing distance. To keep these errors (measuring height, resolution and attenuation) as small as possible, we limit our analysis to a radius of 100 km from each radar site.

c. *Rain gauge data*

We use rain gauge measurements from the Daily Global Historical Climatology Network (GHCN-D) that have good spatial coverage of daily precipitation data in the United States. The main sources for GHNC-D in the United States are the cooperative observer network (COOP) and the Automated Surface Observing System (ASOS) network. The COOP rain gauge network is very extensive, containing 10 000 stations operated by volunteers in the United States (NCEI 2018b). The records extend as far back as 1922. The ASOS network consists of 900 automatic land-based observation stations beginning in 1991 (NCEI 2018b). The HURDAT database, which provides data in a 6-hourly resolution, was used to determine the TC positions (Landsea and Franklin 2013).

Extreme wind conditions are one of the main error sources in rain gauge measurements. Strong wind causes rain drops to fall at an angle, reducing the amount entering the gauges (Sevruk and Nespor 1998). Moreover, nonautomated gauges can overflow in heavy precipitation events (Crow 2017). In the event of a TC, many rain gauges experience outages. In this dataset, the low bias due to high winds is corrected for. The Holland (1980) parametric wind field model, applied to best-track data, is used to estimate the wind speed at each rain gauge 4 times per day. The daily average of this is then used in the following wind correction function:

$$k = \exp\{[-0.001\ln(I_{\mathrm{pd}})] - [-0.0082U_p\ln(I_{\mathrm{pd}})] + [(0.041U_p) + 0.01]\}, \quad (1)$$

where k = conversion factor, I_{pd} = daily rainfall intensity, and U_p = wind speed at 10–12 m above ground during precipitation (Sevruk and Hamon 1984). The correction is applied, regardless of whether a rain gauge is fitted with a wind shield, because only a minority of rain gauges have wind shields and no configuration metadata were available in GHCN-D.

The point measurements from the rain gauges are gridded using the inverse-distance-weighting method. As described in Zhu and Quiring (2017), the definition of neighboring gauges has a large influence on the quality of the interpolation. Here, all gauges within 80 km of each other are considered neighbors, which yields the lowest error over the entire measurement period, when compared to satellite data (Zhu and Quiring 2017). For defining TC precipitation, the moving radius boundary technique (MRBT) is used. In this technique, a certain limit is defined as the radius of TC precipitation. The edges of the radii corresponding to the four TC positions per day are connected to determine the affected area each day (Zhu and Quiring 2017). For this dataset, the limit was initially chosen to be 800 km, as a generous first estimate of TC size.

For this study, the rain gauge data are constrained to a 100-km radius around the available radar stations so as to better compare with the radar data. The gauge data provide a substantially longer record of observations and allow us to make independent estimates of TC rainfall that can be compared with the radar estimates.

d. *Synthetic track model*

A large set of synthetic TCs was generated for each radar site to estimate frequencies of TC precipitation using the technique of Emanuel et al. (2008) applied to NCEP–NCAR reanalyses (Kalnay et al. 1996) over the period 1995–2016. Previous experience with downscaling multiple reanalyses datasets shows small differences in the final results (Emanuel 2017). Broadly, the technique begins by randomly seeding with weak protocyclones the large-scale, time-evolving state given by the reanalysis data. These seed disturbances are assumed to move with the reanalysis, which provided large-scale flow in which they are embedded, plus a westward and poleward component owing to planetary curvature and rotation. Their intensity is calculated using the Coupled Hurricane Intensity Prediction System (CHIPS; Emanuel et al. 2004), a simple axisymmetric

hurricane model coupled to a reduced upper-ocean model to account for the effects of upper-ocean mixing of cold water to the surface. Applied to the synthetically generated tracks, this model predicts that a large majority of them dissipate because of unfavorable environments. Only the "fittest" storms survive; thus the technique relies on a kind of natural selection. Extensive comparisons to historical events by Emanuel et al. (2008) and subsequent papers provide confidence that the statistical properties of the simulated events are in line with those of historical tropical cyclones.

We created separate sets of 4400 synthetic TCs (200 per year) passing within 300 km of each of the selected points of interest (POIs), corresponding to radar locations. This selects all TC tracks that are likely to produce precipitation within 100 km of the POI. The seeding rate for each event set is calibrated to the observed TC frequency of that set using best-track wind data. Next, the revised TCR algorithm is used to estimate the rainfall occurring from the synthetic TCs. The properties of the algorithm are explained in more detail in the following section. From this modeled TC precipitation, the frequencies of rainfall are calculated.

PRECIPITATION ALGORITHM TCR

As Zhu and Quiring (2013) and Lu et al. (2018) describe, the TCR algorithm uses the net vertical velocity and the saturation specific humidity to calculate the vertical vapor flux, and this, multiplied by a precipitation efficiency, is assumed to equal the precipitation rate. Although the vertical velocity is a model variable, it is poorly resolved outside the inner core and is not recorded. Additionally, topographical effects and asymmetric vertical motion owing to interactions between the TC and environmental flow and surface friction are not accounted for in the model itself. Instead, we here estimate the vertical velocity using simple boundary layer physics and the vorticity equation applied to time-evolving balanced flow, as described in detail by Lu et al. (2018). We provide a brief summary here.

In the first step, the theoretical radial profile of azimuthal wind developed by Emanuel and Rotunno (2011) is fitted to the maximum wind speed and radius of maximum winds, and modified by adding a function of the environmental flow. This is necessary, as CHIPS is computed in potential radius coordinates, which has poor resolution outside of the eyewall. Moreover, the large number of tracks forces one to carefully select the essential output data of CHIPS. The vertical velocity is then estimated at any point within the storm's wind field by summing five components due respectively to topography, boundary layer convergence, storm vorticity changes, baroclinic interactions, and radiative cooling.

First, the vertical velocity at the surface is calculated as the dot product of the boundary layer wind vector and the slope of the topography, here represented by a $0.25° \times 0.25°$ dataset. Next, the vertical velocity at the top of the boundary layer is calculated from the surface vertical velocity together with the convergence of the Ekman flow in the boundary layer. The time evolution of the free tropospheric TC vorticity is assumed to be due mostly to the stretching term in the vorticity equation, from which the difference between midtropospheric and boundary layer vertical velocity may be inferred. A baroclinic component is added by considering the interaction of the TC vortex with environmental shear. This is estimated as the dot product of the gradient wind with the slope of the background isentrope. As a result, a region of ascent forms downshear of the vortex, consistent with observations.

In the entire region of the vortex, a gentle subsidence that results from radiative cooling is added to the other four components. This subsidence is here set to a spatially uniform value of $-0.005\,\mathrm{m\,s^{-1}}$. Once the midtropospheric vertical velocity is calculated, it is multiplied by the saturation specific humidity of the lower troposphere and a fixed precipitation efficiency of 0.9 to yield precipitation. Precipitation is set to zero if this procedure yields a negative value. The estimated values of subsidence and precipitation efficiency are based on Lu et al. (2018).

The largest component is usually the frictionally induced upward motion at the top of the boundary layer. Here we improve upon earlier work by using drag coefficients for a neutrally stratified atmosphere calculated from a $0.25° \times 0.25°$ surface roughness dataset obtained from the European Centre for Medium-Range Weather Forecasts (ECMWF), rather than using a constant coefficient. Not surprisingly, this was found to have substantial effects on the calculation of boundary layer convergence away from the coast.

e. Selection of points of interest

We selected radar stations experiencing a reasonably regular occurrence of TCs (Konrad and Perry 2009). This includes the coastal areas of the Gulf of Mexico as well as the Atlantic coastline extending as far north as New York City, New York. As CHIPS and TCR may not handle extratropical transition very well (Emanuel et al. 2004; Lu et al. 2018), we limited the analysis to areas where TCs usually have not yet transitioned to extratropical storms. The analyzed stations also extend several 100 km inland, as decaying TCs can still produce heavy precipitation (Rappaport 2014). We consider rainfall within a 100-km radius of the POIs. Figure 1 provides an overview of all locations analyzed.

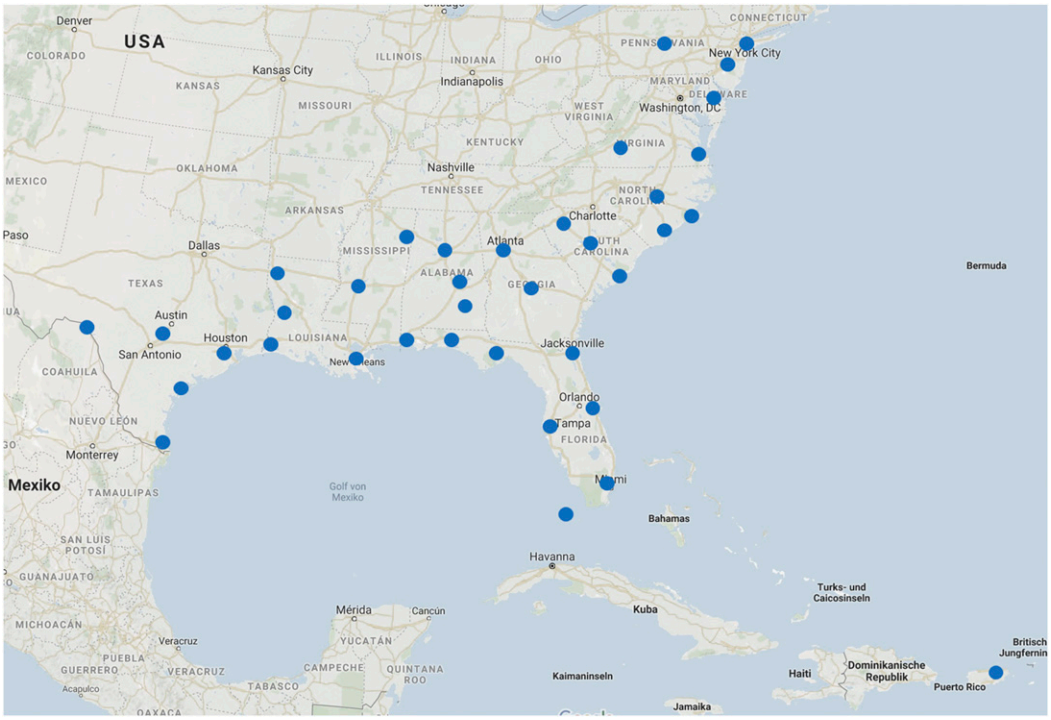

FIG. 1. Selected points of interest.

3. Methods

a. *Identifying TC precipitiation in observational data*

A common metric of TC size is the radius of the outermost closed isobar. As Matyas (2010) describes, the ROCI encompasses the area of TC-related rainfall in 90% of all cases. While this means that the area within the ROCI can exceed the actual area of TC precipitation, rarely any precipitation is unaccounted for. Therefore, here the ROCI is used as a direct measure to determine the area of TC-associated rainfall. To avoid including small, unrelated precipitation events, the lower limit of a TC precipitation event is defined as 10-mm storm total precipitation. Data associated with TC rainfall at a certain POI is thus required to be within 100 km of a POI, within the ROCI of a TC at a given time, and to exceed 10 mm over the lifetime of the event. To determine the distance between a TC and a POI at any given time, the best-track storm center position is linearly interpolated to the required time of interest. This is especially relevant for the radar data, as they are measured in small, varying time intervals. This approach follows the same principle as the MRBT described in Zhu and Quiring (2017), with the ROCI as the defined limit. The MRBT method uses a moving circle around the TC location to identify affected areas. The radar data, as well as the rain gauge data, are processed in this way, so that predominantly TC-associated rain remains. It is important to note that the rain gauge data have a daily temporal resolution and thus take into account the entire area affected by a TC during a day, whereas the radar data only take into account the area affected by a TC precisely at the time of the measurement. This difference may cause the rain gauge data to include non-TC precipitation. As the rain gauge dataset was initially limited to 800 km around a TC, in the vast majority of cases it can be additionally constrained to the ROCI without loss of data. Only in one case does the ROCI in the best-track data exceed 800 km, while the TC is in range of a POI. For radar data, the affected area is analyzed at the time of each measurement, discarding previously affected areas as soon as they are no longer within the ROCI. The daily resolution of the rain gauge data introduces a source of error, as the exact beginning and end of the TC cannot be taken into account. If another precipitation system is very close to the ROCI of a TC, it might get classified as TC precipitation. In general, this error tends to be small, as convection tends to be suppressed in the outer regions of TCs because of the upper-level anticyclone.

b. *Spatial character of data*

While it is not practical to evaluate radar, rain gauge, and model data at every grid point available, we still want to retain some spatial information. For every storm, the area of most interest and highest immediate

impact is the area of largest storm total precipitation. The runoff from these areas can lead to flooding in other areas, but this is outside the scope of this study. To reduce the effect of areas that were affected by single convective cells, which are not resolved by the model, area averages of 0.5° × 0.5° are made around every grid point of the 0.1° × 0.1° grid. Out of these area averages, the maximum precipitation is selected, representing that 0.5° × 0.5° area within the observational scope that received the most precipitation during a particular event. We apply this selection, as maximum precipitation can often be spatially constrained and the average of the entire area would not represent the impact of the precipitation satisfactorily. This method is applied to all three datasets.

c. *Statistical methods*

Here we describe the methods we use to quantify the exceedance frequency of rainfall and the associated sampling uncertainty associated with the two observational datasets.

1) EXCEEDANCE FREQUENCY

The exceedance frequency describes the annual frequency at which an event larger than a certain magnitude occurs. It can be obtained by estimating an empirical cumulative distribution function (CDF). To obtain the CDF, we calculate the exceedance frequency f of each event x at a POI. This yields the empirical CDF:

$$f(x) = n_{\text{exc}}(x)/T, \tag{2}$$

where f = exceedance frequency, x = storm total precipitation of event, n_{exc} = number of exceedances and T = total length of observation period

2) ERROR CALCULATION

The relative root-mean-square error (rRMSE) and relative mean absolute error (rMAE) are statistical methods of quantifying the difference between two datasets. The relative error is defined as the relative residual between the actual data D and the predicted values D':

$$r\text{RMSE} = \left[\overline{\left(\frac{D - D'}{D}\right)^2}\right]^{1/2} \quad \text{and} \tag{3}$$

$$r\text{MAE} = \overline{\left|\frac{D - D'}{D}\right|}. \tag{4}$$

We later use the rRMSE and rMAE to quantify the difference in event frequency f between both observational datasets [section 4a(1)]. The rRMSE is sensitive to outliers and will favor predictions that avoid large deviations from the actual values.

3) MODEL SAMPLING UNCERTAINTY

The synthetic track data constitute a much larger sample than the observational data, which, owing their paucity, suffer from substantial sampling uncertainty. To quantify this uncertainty, the 90% confidence interval around the model frequencies is determined, using the inverse CDF of a Poisson distribution based on the expected number of observations, given the synthetic track rate and the number of years in the observational datasets.

4) MEASUREMENT GAPS

As both radar and rain gauges can suffer extreme conditions during a TC, they are prone to outages. Since the radar data have relatively high time resolution, even short measurement gaps of less than a day can be identified. If the gaps in the radar data are less than 2 h, they are interpolated from the adjoining measurements. As the radar measurements in the 1990s are in hourly intervals, the choice of 2 h is a compromise between making use of as much data as possible and accounting for the temporal variability of precipitation. Since the temporal variability of rainfall is very high, longer stretches of time cannot be interpolated without missing potential heavy rainfall. If the gap exceeds this length, this time span will be defined as missing. By subtracting the missing minutes from the length of the event (Δt_{events}), the cumulative length of viable measurements is defined ($\Delta t_{\text{measurements}}$). The temporal fraction of viable measurements (correction factor C) can then be used to readjust the frequency of events when calculating the frequencies:

$$C = \Delta t_{\text{events}}/\Delta t_{\text{measurements}} \quad \text{and} \tag{5}$$

$$f_{\text{adjusted}} = f_{\text{observed}} C. \tag{6}$$

This approach assumes that the missing measurements are similar to all obtained measurements. This implies the additional assumption that measurements outages occur randomly during an event. Using this method, the missing time spans are compensated for from all viable measurements over all events. Since the rain gauge data are only recorded daily and have already been interpolated across measurement gaps, no compensation of this kind is required. However, storms that are missing completely, according to the best-track record, are identified, and the frequency is upscaled accordingly.

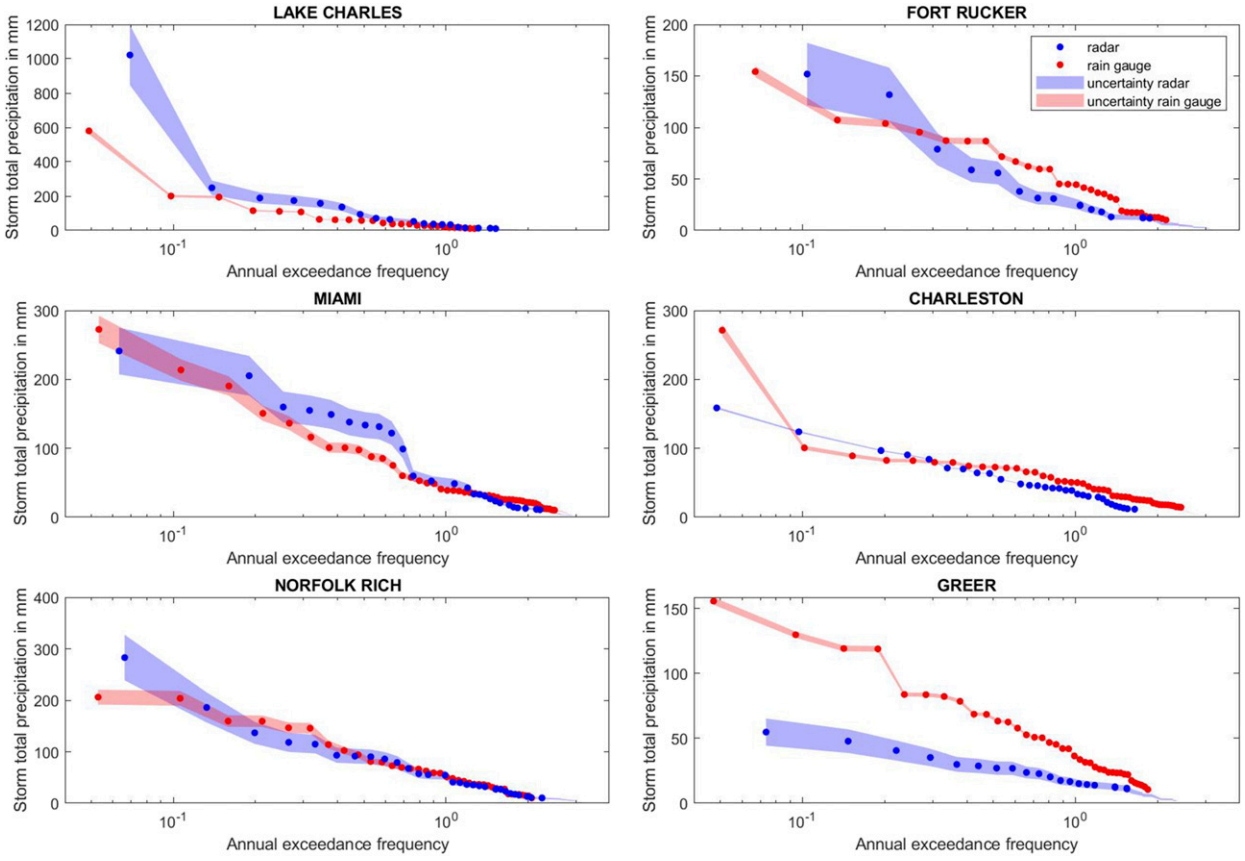

FIG. 2. Comparison of radar- and rain gauge–derived frequencies within the same observation period (~25 yr; for the exact range see Table 1 under years of radar data). The uncertainty resulting from missing data is shown by shading. Note that the axes are different for different POIs.

4. Results

a. Comparison of observational datasets

Since the rain gauge data have previously been compared with satellite and modeled data (Zhu and Quiring 2017), their caveats very well known. Even though they are corrected for wind speed effects, they still tend to miss the peak precipitation of events because of their point-measurement nature (Zhu and Quiring 2017). The radar data, on the other hand, have their own caveats, as described in section 2b. This dataset is available from Feldmann (2019). In the following both datasets are compared with each other.

1) COMPARISON OF IDENTICAL OBSERVATION PERIODS

Figure 2 shows a comparison of exceedance frequency curves calculated from the rain gauge and radar datasets, for six POIs, selected to represent the geographical distribution of all POIs: Lake Charles, Louisiana, represents the northwestern Gulf Coast; Fort Rucker, Alabama, represents the inland region of the northeastern Gulf Coast; Miami, Florida, represents the southern Gulf Coast; Charleston and Greer, South Carolina, represent the coast and inland regions of the Carolinas; and Norfolk–Richmond, Virginia, represents the mid-Atlantic coastal area. The results at other POIs are shown in the online supplementary material. The shading represents the percentage of missing radar or rain gauge data at each POI. Here, the rain gauge dataset has been restricted to the observation period of the radar data to yield copacetic comparisons.

In most cases, the radar and rain gauge data line up very well. While rain gauge data often show higher precipitation at higher frequencies (Fort Rucker, Miami, and Charleston), the radar data tend to show somewhat higher precipitation at lower frequencies (Lake Charles, Fort Rucker, and Miami). Because the rain gauge data have only daily resolution, in contrast to the much finer resolution of the radar data, they might include non-TC precipitation that occurred within the same day as a TC event. The higher values of extreme precipitation estimated by radar are likely due to their better area coverage and better functionality in high

TABLE 1. Quality of observational data: fraction of available measurements for radar and rain gauge data, and relative differences in frequencies between radar and rain gauge data. Italics indicate problem data: an rMAE $> 0.5\,\mathrm{yr}^{-1}$ indicates that caution is advised, and an *r*MAE $> 0.9\,\mathrm{yr}^{-1}$ indicates that the data are not recommended for use (locations marked with an asterisk).

	Data availability					
	Rain gauge		Radar		Frequency error	
Point of interest	Percent	Yrs	Percent	Years	rMAE	rRMSE
Atlanta (GA)	*94.9*	*1922–2017*	*72.5*	*1995–2017*	*0.878*	*1.061*
Austin/San Antonio (TX)	97.1	1922–2017	72.1	1995–2017	0.400	0.434
Birmingham (AL)	*96.4*	*1922–2017*	*72.5*	*1995–2017*	*0.898*	*1.617*
Brownsville (TX)	*81.6*	*1922–2017*	*82.6*	*1995–2017*	*0.772*	*0.824*
Charleston (SC)	93.8	1922–2017	91.0	1996–2017	0.369	0.431
Columbia (SC)	*94.0*	*1922–2017*	*77.7*	*1995–2017*	*0.718*	*0.862*
Columbus Air Force Base (MS)	95.8	1922–2017	63.4	2001–17	0.193	0.241
Corpus Christi (TX)	89.0	1922–2017	77.0	1998–2017	0.415	0.532
Dover Air Force Base (DE)	81.6	1922–2017	64.2	2001–17	0.446	0.588
Eglin Air Force Base (FL)	94.5	1922–2017	74.2	2001–17	0.379	0.485
Fort Polk (LA)	*92.5*	*1922–2017*	*59.0*	*2001–17*	*0.554*	*0.642*
Fort Rucker (AL)	*93.1*	*1922–2017*	*67.6*	*2001–17*	*0.581*	*0.672*
**Greer (SC)*	*96.2*	*1922–2017*	*61.8*	*1995–2017*	*2.662*	*3.782*
Houston (TX)	89.6	1922–2017	74.3	1995–2017	0.303	0.351
Jackson/Brandon (MS)	95.6	1922–2017	71.2	2003–17	0.398	0.476
Jacksonville (FL)	88.6	1922–2017	79.5	1995–2017	0.374	0.510
**Key West (FL)*	*61.3*	*1922–2017*	*80.1*	*1996–2017*	*0.965*	*0.966*
Lake Charles (LA)	92.8	1922–2017	70.2	1995–2017	0.619	0.708
Laughlin Air Force Base (TX)	94.3	1922–2017	71.3	2002–17	0.341	0.432
Maxwell Air Force Base (AL)	96.7	1922–2017	66.2	2001–17	0.521	0.662
Melbourne (FL)	85.2	1922–2017	84.9	1995–2017	0.445	0.550
Miami (FL)	85.4	1922–2017	81.2	1995–2017	0.226	0.279
Mobile (AL)	92.9	1922–2017	70.8	1995–2017	0.396	0.531
Morehead City (NC)	91.1	1922–2017	78.8	1995–2017	0.233	0.284
New Orleans (LA)	89.9	1922–2017	70.6	1995–2017	0.226	0.313
New York (NY)	75.5	1922–2017	58.0	1995–2017	0.306	0.357
Norfolk/Richmond (VA)	85.9	1922–2017	80.1	1995–2017	0.491	0.640
Philadelphia (PA)	78.6	1922–2017	71.2	1995–2017	0.825	1.120
Raleigh/Durham (NC)	94.1	1922–2017	83.0	1995–2017	0.270	0.339
Roanoke (VA)	*93.6*	*1922–2017*	*80.1*	*1995–2017*	*0.542*	*0.627*
Robins Air Force Base (GA)	94.5	1922–2017	67.4	2001–17	0.374	0.580
San Juan (PR)			84.1	2001–17		
Shreveport (LA)	96.5	1922–2017	66.5	1998–2017	0.449	0.584
State College (PA)	86.7	1922–2017	68.6	1995–2017	0.771	0.975
Tallahassee (FL)	*91.4*	*1922–2017*	*67.7*	*1995–2017*	*0.520*	*0.646*
Tampa (FL)	83.9	1922–2017	79.1	1995–2017	0.438	0.709
Wilmington (NC)	*88.4*	*1922–2017*	*86.2*	*1995–2017*	*0.621*	*0.717*

winds. As the precipitation extremes are mostly from intense storms, the rain gauge data are likely to be more uncertain for such events.

In Greer, the radar data substantially underestimate the gauge-measured precipitation over the whole range of frequencies. However, Greer is missing 38.2% of TC radar precipitation measurements. When too many relevant data are missing, rescaling the frequency may not accurately account for the lack of data. In this case, the use of the radar data is not recommended.

To summarize the quality of the datasets, Table 1 shows the completeness of both radar and rain gauge data, as well as their *r*MAE and *r*RMSE of frequency. POIs in italics have a difference in frequency that is greater than $0.5\,\mathrm{yr}^{-1}$. Because the difference is considerable, the data need to be used with caution. POIs that are not recommended for this analysis are indicated in italics and with an asterisk, because they show large differences in frequency ($>0.9\,\mathrm{yr}^{-1}$) during the same observational period.

Key West, Florida, and Greer, as mentioned above, have serious deficiencies in either radar or rain gauge data coverage. At this level, the frequency rescaling method is insufficient to properly account for the missing data. Discrepancies also result from the inherent differences between the measurement methods. For example, the rain gauges are still point-based in nature;

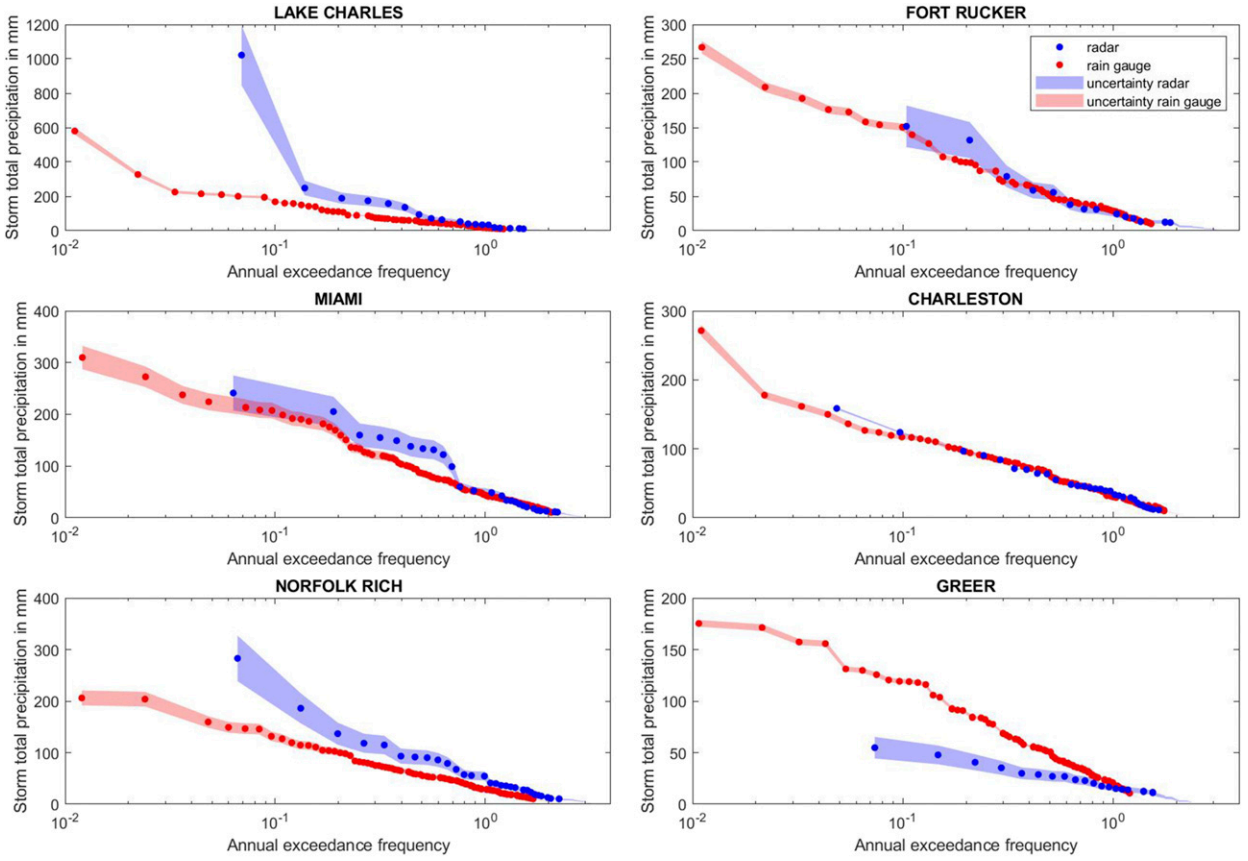

FIG. 3. As in Fig. 2, but during the complete observation period (~25 yr for radar data, and ~95 yr for rain gauge data; for the exact range see Table 1).

therefore, they can miss the precipitation peak of an event if it passes in between them.

2) COMPARISON OF COMPLETE RECORDS

Since the rain gauge data extend much further back in time, they present an opportunity to examine event frequencies on different time scales. Figure 3 shows that while many POIs still line up very well, the length of the record is of great importance. If the largest events have occurred during the radar observation period, they show up with a considerably higher frequency than in the rain gauge dataset (e.g., Lake Charles and Norfolk–Richmond). This illustrates that estimating the frequency of events that only occur sporadically during the respective observation periods of each dataset is challenging. For example, an event like Hurricane Harvey (>500-mm storm total precipitation), which affected the Lake Charles area (Fig. 3, top right), is a ≥25-yr event ($\geq 0.041\,\mathrm{yr}^{-1}$) in the radar data, but a ≥100-yr event ($\geq 0.010\,\mathrm{yr}^{-1}$) in the rain gauge data. Model analyses suggest that it likely is an ~325-yr event ($0.003\,\mathrm{yr}^{-1}$) (Emanuel 2017). This also poses a problem when comparing radar- and gauge-based frequencies with those based on the TCR-model-based estimates, which are based on far more data.

Another noticeable feature is the difference in maximum frequency at some stations (e.g., Lake Charle, Fort Rucker, Norfolk–Richmond, Greer). The maximum frequency shows the overall event frequency of any TC precipitation occurring. The difference between the datasets may in part reflect the nonstationarity of TC frequency. Especially when comparing estimates based on a long record to those based on a shorter one, chances are that the shorter period happened to fall in a period of higher or lower activity than on average.

b. Model performance

When comparing TCR-based frequencies with those deduced from observations, several deficiencies become evident. For one, almost all stations show a strong offset in high-frequency, low-rainfall events (e.g., Fig. 5, described in more detail below), while there is a better fit in the midrange of frequencies. Some stations also show vastly different slopes in observational and modeled

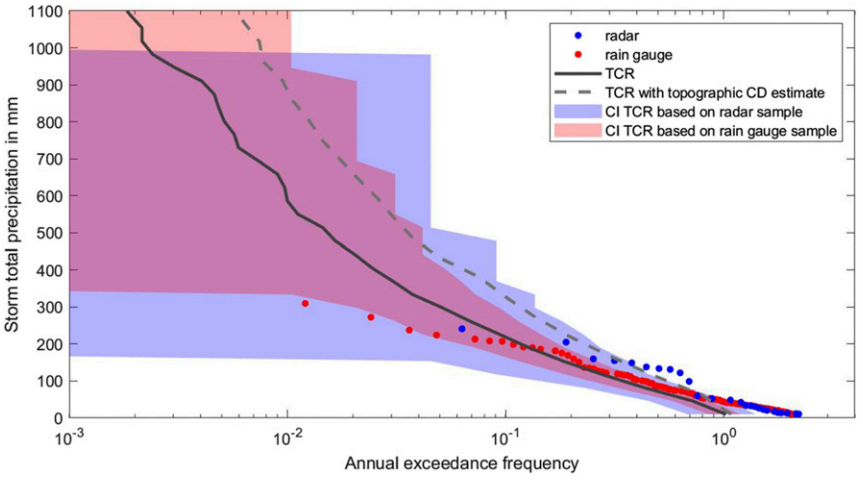

FIG. 4. Comparison of radar- and rain gauge–derived frequencies with those derived from the TCR algorithm applied to 4400 events affecting Miami. The model-derived estimate based on the earlier version of TCR with topographically determined drag coefficients is shown by the dashed gray line. Estimates of the sampling uncertainty of the TCR data with respect to the radar and rain gauge data are shown by blue and pink shading, respectively.

frequencies (e.g., Fig. 4). Very few show a consistent offset over the entire range. Since the two observation-based frequency curves agree quite well at most stations, these differences are likely deficiencies of the model and not of the observational data. In the following, we suggest and evaluate possible sources of model error.

1) IMPROVING THE DRAG COEFFICIENT

The TCR algorithm is highly sensitive to the choice of the surface roughness coefficient as it directly influences the magnitude of the frictionally induced inflow (Lu et al. 2018). We previously assumed that the variations in the drag coefficient, CD, are a linear function of topographic height. The linear estimate implemented in the model works well for many stations, but shows large deficiencies in inland areas with high elevation and flat terrain and also in other areas with variations in surface roughness unrelated to topography, but rather surface properties. To improve the performance, we here used surface roughness values at a resolution of 0.25° × 0.25°, provided by ECMWF. The neutral drag coefficient that we apply to the gradient wind is then estimated, loosely following Esau (2004), as

$$C_D' = \left[\frac{k}{\ln(500/z_0)}\right]^2 \quad \text{and} \tag{7}$$

$$C_D = 0.9\frac{C_D'}{1 + 50C_D'}, \tag{8}$$

where k is von Kármán's constant, here taken to be 0.35.

This formulation of the drag coefficient directly affects the slope of the model-derived frequency curves, as it proportionally affects the precipitation rate. We apply the drag coefficient [Eq. (8)] not only in the TCR algorithm but also to the CHIPS model simulations, in which it affects the rate of decay of TCs and thus also their overall frequency at inland locations. An example of the improvement in model performance can be seen in Fig. 4. Miami, a flat coastal area, was previously assigned too large a drag coefficient, creating a frequency distribution much steeper than observed. The use of surface roughness greatly improves the model performance and observed events now lie within the 90% confidence interval of the sampling uncertainty. Similar behavior can be seen for Key West; Tallahassee, Florida; and Houston, Corpus Christi, and Brownsville, Texas. These are also flat coastal areas with low surface roughness. Hereinafter, all figures are based on TCR calculations with the improved drag coefficient.

2) BACKGROUND PROBABILITY OF PRECIPITATION

The ROCI, while it is one of the few readily available size metrics, has shortcomings, as described by Knaff et al. (2014). There is no consistent method to determine it, and most methods include subjective choices that are not always well documented. Moreover, the ROCI is influenced by the ambient pressure field and can be enlarged or diminished by several means. As Matyas (2010) states, in 90% of cases the ROCI includes or exceeds the area of TC-related precipitation. This leads to additional non-TC-related areas that are included

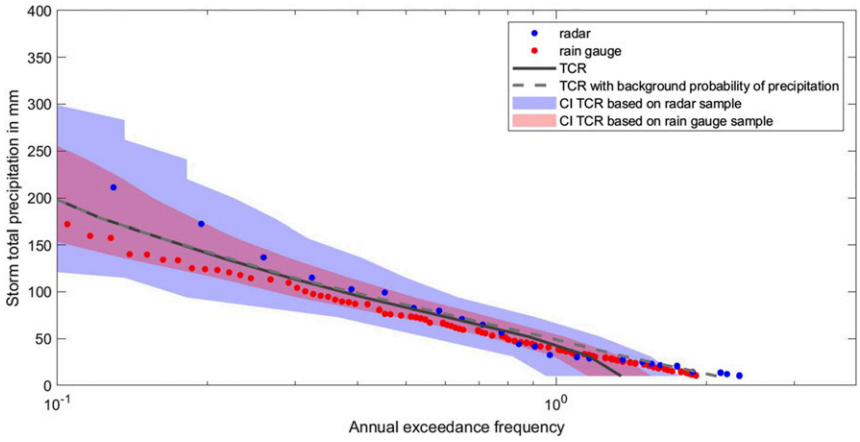

FIG. 5. Comparison of radar- and rain gauge–derived frequencies with those derived from the TCR algorithm applied to 4400 synthetic tracks affecting Jacksonville. The gray dashed line shows the model-derived frequencies modified to include the background probability of precipitation in summer months. Estimates of the sampling uncertainty of the TCR data with respect to the radar and rain gauge data are shown by blue and red shading, respectively.

within the ROCI in the majority of observed cases. The precipitation within this nonrelated area should correspond to the general probability of precipitation (e.g., in the form of summer thunderstorms) occurring on a normal day. Such background precipitation is not accounted for by the TCR algorithm. To determine whether this is an important factor in the discrepancies, the background frequency of precipitation is added to the TC precipitation frequency produced by the model. To obtain the background probability of precipitation, we use the daily precipitation records for the summer months of 15 years (2000–14) (NCEI 2018b). We eliminate days associated with TCs from the dataset. After calculating the exceedance frequency, we rescale it to the number of TC days. This yields the background probability of precipitation and is added to the frequency obtained by the TCR algorithm. As shown in the case of Jacksonville, Florida (Fig. 5), this effectively narrows the gap between observed and modeled frequency in the low-frequency range. However, the TCR algorithm still underestimates the observed frequency. This assumption has also been tested for Lake Charles, Charleston, Norfolk–Richmond; Laughlin and San Antonio, Texas; and Atlanta, Georgia (not shown). They all show qualitatively the same improved TCR exceedance frequencies after addition of the background probability of precipitation, but still underestimate the observation-derived exceedance frequencies.

3) WIND FIELD MODEL

We use the theoretical wind field profile developed by Emanuel and Rotunno (2011), which is also used in Zhu and Quiring (2013). This profile should only be valid in the inner core, but we here use it everywhere. As described in Emanuel and Rotunno (2011) and Chavas and Lin (2016), this wind profile tails off too sharply in the outer region, where it should be matched to an outer wind profile. This would produce more rain in the outer regions and may also help to explain the discrepancies between model predictions and observations in the high-frequency, low-intensity regime. Currently, outer wind profiles are not analytically solvable and thus incur a computational expense, when applied to large track sets. Since it is more essential to represent the core for the high-impact events, the accuracy of the outer region is sacrificed in favor of keeping computational resources to a minimum.

4) MODEL PERFORMANCE IN DIFFERENT REGIONS

We applied our modeling approach to all POIs, covering the U.S. coastline from Texas to New York City, as well as several inland locations. We emphasize the comparison with the rain gauge-derived estimates in the frequency range from 0.03 to 0.3 yr^{-1} to avoid both the very large observational sampling uncertainty at the low-frequency end of the spectrum and the aforementioned issues with the TCR approach at the high-frequency end of the spectrum. Figure 6 provides an overview of TCR's performance in different regions. The radar and rain gauge data are used from their respective complete observational periods, resulting in available data for ~25 and ~95 yr. The results at other POIs are presented in the online supplementary material.

Lake Charles, which is relatively far west, shows good agreement throughout the entire range of rain gauge data. The radar data lie near or just above the 90% confidence

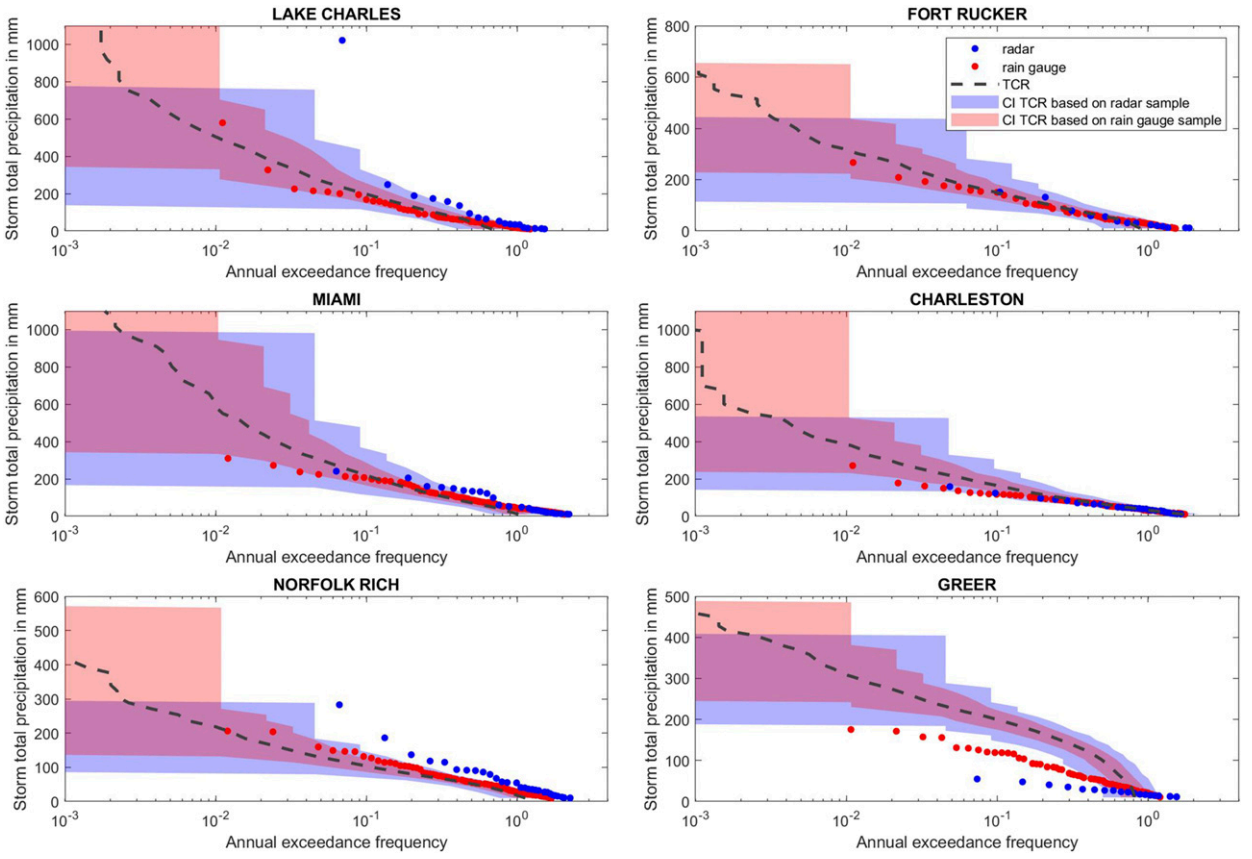

FIG. 6. Comparison of radar- and rain gauge–derived frequencies data with those derived from the TCR- algorithm applied to 4400 synthetic tracks affecting six radar sites. Estimates of the sampling uncertainty of the TCR data with respect to the radar and rain gauge data are shown by blue and red shading, respectively. Note that the axes are different for different POIs.

bound of the TCR sampling uncertainty, except for the largest event, which was the storm total precipitation of Hurricane Harvey. Because of the relatively short time span of radar measurements, and perhaps an upward trend in TC rainfall, Hurricane Harvey shows up as a more frequent event than indicated by the longer-term gauge data.

Fort Rucker, farther inland along the eastern part of the Gulf Coast, shows very good agreement for both rain gauge and radar data. Both observational datasets lie within the 90% confidence interval of the TCR data. Miami's annual exceedance frequencies also show good agreement between the TCR algorithm and the observations. The improvement of the drag coefficient alleviated the previously observed strong difference in the slope of the model-derived frequencies. Similar results are found for the rest of coastal Florida and coastal Texas. Charleston, on the coast of South Carolina, shows good model performance. Both the radar and the rain gauge data lie almost exclusively inside their sampling confidence intervals.

Farther north, modeled frequencies show less agreement with the radar data; however, the agreement with the rain gauge data remains good. At Norfolk, almost all radar data lie outside the sampling error bounds, whereas all rain gauge data lies within the error bounds. This suggests that this region may have experienced a short-term (20 yr) trend with an elevated TC rainfall frequency. As Fig. 2 shows, rain gauge and radar data otherwise agree very well within the same observation period.

In general, the size of a TC is increasingly difficult to define at higher latitudes, since baroclinicity causes asymmetries in the shape that are not accounted for in the MRBT method. Nonetheless, modeled and observed results agree quite well in this region.

Greer, lying farther inland in South Carolina, also shows strong disagreement, but in this case there are strong gradients in surface roughness. Since the model data are evaluated in a similar way as the observation data and the maximum storm total precipitation is selected, the high surface roughness values may have a disproportionally large impact. A possible solution could be to use a smoothed surface roughness grid. In general, the TCR reacts very sensitively to changes in surface roughness. The effects of larger surface

roughness are also not advected with the wind field, but only affect the rain rate directly above, which leads to very abrupt changes in precipitation intensity. This effect was also described in Lu et al. (2018).

5. Conclusions

We analyzed and compared three methods of estimating frequencies of TC rainfall. Rainfall frequencies sourced from rain gauge and radar data largely support each other and work best for high event frequencies with low intensities. Even though they both present substantial measurement uncertainties under TC conditions and have strongly differing properties, the frequency estimates generally agree quite well. The inherent uncertainty of estimating the frequency of an event that occurs only very few times during the observation period is the main limitation of the radar data and, to some extent, the rain gauge data. While the ~90 yr of gauge records substantially exceed the ~20 yr of radar records, the truly extreme events with the highest impacts tend to occur less frequently than every 90 yr. Being able to correctly estimate lower exceedance frequencies is one of the advantages of estimating rainfall frequencies using the TCR algorithm applied to large sets of synthetic TCs: By this means, one can generate enough events to calculate the tail of the frequency distribution to a range of frequencies around $10^{-4}\,\mathrm{yr}^{-1}$, which relies on physical principles rather than statistics. When we evaluate model results in the middle range of the distributions (frequencies of 0.3–0.03 yr^{-1}), we see that most coastal locations perform very well, especially along the Gulf Coast and the southern part of the Atlantic Coast. Farther inland, the TCR algorithm seems to experience difficulties in representing areas with large gradients in surface roughness. Moreover, locations with very few recorded events have large sampling uncertainty, and thus, not surprisingly, show less agreement between TCR data and observational data. However, inland locations not affected by sparse events or large gradients in surface roughness also perform very well. The POIs in higher latitudes need to be considered carefully, since the ROCI as the definition of the area affected by TC precipitation is more problematic, as TCs become more asymmetric. Nevertheless, this region shows good agreement between the rain gauge data and the modeled data, suggesting a good representation of the long-term conditions. Discrepancies between the long-term rain gauge data and short-term radar data indicate that this region has had a higher overall occurrence frequency of TCs within the last 20 yr.

Given these caveats, the TCR algorithm applied to synthetic TC tracks achieves good agreement with observational records at the majority of analyzed locations. It provides a powerful tool to estimate the tail of the event frequency distribution for the high-impact events that cause the most damage. Essential to its functionality are good estimates of the drag coefficient and reasonably accurate renditions of the wind profile.

Acknowledgments. We thank the experts who provided advice, information, and data for this project; Dr. James Kurdzo gave us further insight into the pitfalls and particularities of radar measurements. Moreover, we thank the National Centers for Environmental Information for the accessability of their data. In addition, we are very grateful to Tom Beucler, Jonathan Lin, and Matthias Feldmann for assisting us with computational challenges during our work. Moreover, we thank Dr. Christopher Landsea, as well as two anonymous reviewers, for providing insightful reviews and helping to improve this work. We also thank the Zeno Karl Schindler Foundation for supporting Monika Feldmann's work, as well as National Science Foundation Grant AGS-1520683 for supporting Prof. Kerry Emanuel. A special thank you goes to Kerry Emanuel and Ulrike Lohmann for supporting Monika Feldmann in this exciting master thesis exchange project at MIT and for the excellent supervision.

REFERENCES

Blake, E. S., and D. A. Zelinsky, 2018: Hurricane Harvey (AL092017) 17 August–1 September 2017. National Hurricane Center Tropical Cyclone Rep., 77 pp., https://www.nhc.noaa.gov/data/tcr/AL092017_Harvey.pdf.

Chavas, D. R., and N. Lin, 2016: A model for the complete radial structure of the tropical cyclone wind field. Part II: Wind field variability. *J. Atmos. Sci.*, **73**, 3093–3113, https://doi.org/10.1175/JAS-D-15-0185.1.

Crow, B., 2017: When rain gauges overtop: A collection of reports exceeding the CoCoRaHS 11″ gauge capacity. Metstat, https://metstat.com/cocorahs-11-inch-reports/.

Curry, G. R., 2012: *Radar Essentials: A Concise Handbook for Radar Design and Performance Analysis.* SciTECH Publishing, 133 pp.

Demuth, J. L., M. DeMaria, and J. A. Knaff, 2006: Improvement of Advanced Microwave Sounding Unit tropical cyclone intensity and size estimation algorithms. *J. Appl. Meteor. Climatol.*, **45**, 1573–1581, https://doi.org/10.1175/JAM2429.1.

Emanuel, K., 2017: Assessing the present and future probability of Hurricane Harvey's rainfall. *Proc. Natl. Acad. Sci. USA*, **114**, 12 681–12 684, https://doi.org/10.1073/pnas.1716222114.

——, and R. Rotunno, 2011: Self-stratification of tropical cyclone outflow. Part I: Implications for storm structure. *J. Atmos. Sci.*, **68**, 2236–2249, https://doi.org/10.1175/JAS-D-10-05024.1.

——, C. DesAutels, C. Holloway, and R. Korty, 2004: Environmental control of tropical cyclone intensity. *J. Atmos. Sci.*, **61**, 843–858, https://doi.org/10.1175/1520-0469(2004)061<0843:ECOTCI>2.0.CO;2.

——, R. Sundararajan, and J. Williams, 2008: Hurricanes and global warming: Results from downscaling IPCC AR4

simulations. *Bull. Amer. Meteor. Soc.*, **89**, 347–367, https://doi.org/10.1175/BAMS-89-3-347.

Esau, I. N., 2004: Parameterization of a surface drag coefficient in conventionally neutral planetary boundary layer. *Ann. Geophys.*, **22**, 3353–3362, https://doi.org/10.5194/angeo-22-3353-2004.

Faust, E., and M. Bove, 2018: Serie von Wirbelstürmen in Japan und zwei Volltreffer in USA: Die Bilanz der Wirbelsturmsaison 2018 (Series of hurricanes in Japan and two direct hits in the USA: The balance of the hurricane season 2018). Munich Re, https://www.munichre.com/topics-online/de/climate-change-and-natural-disasters/natural-disasters/storms/hurricanes-and-typhoons-2018.html.

Feldmann, M., 2019: Climatology of rainfall from Atlantic hurricanes in the USA from radar data. Zenodo, accessed 5 August 2018, https://doi.org/10.5281/zenodo.1745239.

Holland, G. J., 1980: An analytic model of the wind and pressure profiles in hurricanes. *Mon. Wea. Rev.*, **108**, 1212–1218, https://doi.org/10.1175/1520-0493(1980)108<1212:AAMOTW>2.0.CO;2.

Houze, R., 2014: *Cloud Dynamics*. 2nd ed. Academic Press, 496 pp.

Jiang, H., and E. J. Zipser, 2010: Contribution of tropical cyclones to the global precipitation from eight seasons of TRMM data: Regional, seasonal, and interannual variations. *J. Climate*, **23**, 1526–1543, https://doi.org/10.1175/2009JCLI3303.1.

Kalnay, E., and Coauthors, 1996: The NCEP/NCAR 40-Year Reanalysis Project. *Bull. Amer. Meteor. Soc.*, **77**, 437–472, https://doi.org/10.1175/1520-0477(1996)077<0437:TNYRP>2.0.CO;2.

Knaff, J. A., S. P. Longmore, and D. A. Molenar, 2014: An objective satellite-based tropical cyclone size climatology. *J. Climate*, **27**, 455–476, https://doi.org/10.1175/JCLI-D-13-00096.1.

Knapp, K. R., M. C. Kruk, D. H. Levinson, H. J. Diamond, and C. J. Neumann, 2010: The International Best Track Archive for Climate Stewardship (IBTrACS). *Bull. Amer. Meteor. Soc.*, **91**, 363–376, https://doi.org/10.1175/2009BAMS2755.1.

Konrad, C., and B. Perry, 2009: Relationships between tropical cyclones and heavy rainfall in the Carolina region of the USA. *Int. J. Climatol.*, **30**, 522–534, https://doi.org/10.1002/joc.1894.

Landsea, C. W., and J. L. Franklin, 2013: Atlantic hurricane database uncertainty and presentation of a new database format. *Mon. Wea. Rev.*, **141**, 3576–3592, https://doi.org/10.1175/MWR-D-12-00254.1.

Lu, P., N. Lin, K. Emanuel, D. Chavas, and J. Smith, 2018: Assessing hurricane rainfall mechanisms using a physics-based model: Hurricanes Isabel (2003) and Irene (2011). *J. Atmos. Sci.*, **75**, 2337–2358, https://doi.org/10.1175/JAS-D-17-0264.1.

Matyas, C. J., 2010: Associations between the size of hurricane rain fields at landfall and their surrounding environments. *Meteor. Atmos. Phys.*, **106**, 135–148, https://doi.org/10.1007/s00703-009-0056-1.

Munich Re, 2018: A stormy year: Topics Geo—Natural catastrophes 2017: Analyses, assessments, positions. Geo Risks Research/Corporate Climate Centre, 70 pp., https://www.munichre.com/site/touch-publications/get/documents_E711248208/mr/assetpool.shared/Documents/5_Touch/_Publications/TOPICS_GEO_2017-en.pdf.

NCEI, 2018a: NOAA Next Generation Radar (NEXRAD) Level 3 products. NOAA, accessed 28 July 2018, https://data.nodc.noaa.gov/cgi-bin/iso?id=gov.noaa.ncdc:C00708.

——, 2018b: U.S. NOAA data. NOAA, accessed 31 July 2018, https://www.ncdc.noaa.gov/data-access.

——, 2019: NOAA's Weather and Climate Toolkit. NOAA, https://www.ncdc.noaa.gov/wct/.

National Weather Service, 2018: Historic Hurricane Florence, September 12-15, 2018. NOAA, https://www.weather.gov/mhx/Florence2018.

Office of the Federal Coordinator for Meteorological Services and Supporting Research, 2017: WSR-88D meteorological observations. Part C: WSR-88D products and algorithms. Federal Meteorological Handbook 11, FCM-H11C-2017, 394 pp., https://www.ofcm.gov/publications/fmh/FMH11/fmh11partC.pdf.

Peduzzi, P., B. Chatenoux, H. Dao, A. De Bono, C. Herold, J. Kossin, F. Mouton, and O. Nordbeck, 2012: Global trends in tropical cyclone risk. *Nat. Climate Change*, **2**, 289–294, https://doi.org/10.1038/NCLIMATE1410.

Rappaport, E. N., 2014: Fatalities in the United States from Atlantic tropical cyclones: New data and interpretation. *Bull. Amer. Meteor. Soc.*, **95**, 341–346, https://doi.org/10.1175/BAMS-D-12-00074.1.

Risser, M. D., and M. F. Wehner, 2017: Attributable human-induced changes in the likelihood and magnitude of the observed extreme precipitation during Hurricane Harvey. *Geophys. Res. Lett.*, **44**, 12 457–12 464, https://doi.org/10.1002/2017GL075888.

Roth, D., 2018: Tropical cyclone point maxima. NOAA, accessed 3 May 2019, https://www.wpc.ncep.noaa.gov/tropical/rain/tcmaxima.html.

Sevruk, B., and W. Hamon, 1984: International comparison of national precipitation gauges with a reference pit gauge. Instruments and Observing Methods Rep. 17, WMO/TD 38, 139 pp., https://library.wmo.int/pmb_ged/wmo-td_38.pdf.

——, and V. Nespor, 1998: Empirical and theoretical assessment of the wind induced error of rain measurement. *Water Sci. Technol.*, **37**, 171–178, https://doi.org/10.2166/wst.1998.0462.

Smith, J. A., D. J. Seo, M. L. Baeck, and M. D. Hudlow, 1996: An intercomparison study of NEXRAD precipitation estimates. *Water Resour. Res.*, **32**, 2035–2045, https://doi.org/10.1029/96WR00270.

van Oldenborgh, G. J., and Coauthors, 2017: Attribution of extreme rainfall from Hurricane Harvey, August 2017. *Environ. Res. Lett.*, **12**, 124009, https://doi.org/10.1088/1748-9326/aa9ef2.

Weinkle, J., C. Landsea, D. Collins, R. Musulin, R. P. Crompton, P. J. Klotzbach, and R. Pielke Jr., 2018: Normalized hurricane damage in the continental United States 1900-2017. *Nature Sustainability*, **1**, 808–813, https://doi.org/10.1038/s41893-018-0165-2.

Wilson, J. W., and E. A. Brandes, 1979: Radar measurement of rainfall—A summary. *Bull. Amer. Meteor. Soc.*, **60**, 1048–1060, https://doi.org/10.1175/1520-0477(1979)060<1048:RMORS>2.0.CO;2.

Yu, Z., Y. Wang, H. Xu, N. Davidson, Y. Chen, Y. Chen, and H. Yu, 2017: On the relationship between intensity and rainfall distribution in tropical cyclones making landfall over china. *J. Appl. Meteor. Climatol.*, **56**, 2883–2901, https://doi.org/10.1175/JAMC-D-16-0334.1.

Zhu, L., and S. M. Quiring, 2013: Variations in tropical cyclone precipitation in Texas (1950 to 2009). *J. Geophys. Res. Atmos.*, **118**, 3085–3096, https://doi.org/10.1029/2012JD018554.

——, and ——, 2017: An extraction method for long-term tropical cyclone precipitation from daily rain gauges. *J. Hydrometeor.*, **18**, 2559–2576, https://doi.org/10.1175/JHM-D-16-0291.1.